



Photodegradation of Amido Black 10b Dye Under Visible Light Using Ni and Zn Ferrite Catalysts Prepared by a Simple Modified Sol–Gel Method

Radwa A. El-Salamony¹ · Wael A. Aboutaleb¹ · Abdelghaffar S. Dhmees¹

Received: 31 October 2022 / Accepted: 29 January 2023 / Published online: 16 February 2023
© The Author(s) 2023

Abstract

The pure α -Fe₂O₃, NiFe₂O₄, and ZnFe₂O₄ were prepared by a simple modified sol–gel method. The prepared catalysts were characterized by X-ray diffraction, transmission electron microscope, surface area, Zeta potential and optical techniques. The ferrite structure of samples is confirmed. The photocatalytic activity was evaluated toward Amido black 10b dye degradation under visible light at different pHs of 4, 8, and 10 for 90 min irradiation time. The photodegradation toward Amido black b10 dye reached maximum value at pH 8, and it reaches 92%, 89%, and 85% over ZnFe₂O₄, Fe₂O₃, and NiFe₂O₄ photocatalysts; respectively. The increased photoactivity of the ZnFe₂O₄ sample can also be attributed to its lower bandgap of 2 eV, the formation of the ⁻OH-surface group. Since ⁻OH can interact with the photoexcited holes that were originally formed on the catalyst surface, hydroxyl radicals are produced that have strong oxidizing properties. Whereas; the dye photodegradation is negligible in the case of Fe₂O₃, and NiFe₂O₄ catalysts at pH 10, due to the electrostatic repulsion between negatively charged catalyst surface and dye ions at high basic medium. While, in case of ZnFe₂O₄, the photodegradation reached only 40%.

Keywords α -Fe₂O₃ · NiFe₂O₄ · ZnFe₂O₄ · Amido black 10b dye · Photodegradation

1 Introduction

Dyes, along decades, have extensively used in wide spectrum of industries. The uncontrolled discharge of untreated hazardous dyes into fresh water causing massive environmental destruction to ecosystem and human health. Therefore, the dyes mineralization in aquatic system has become in a top priority. Photocatalysis technique is an ecofriendly effective method for dyes mineralization. In such technique, the advantageous semiconductors with large specific surface area, chemical stability, and high photocatalytic response are used as catalysts [1, 2]. Iron oxide is a significant material due to their high catalytic activity, biocompatibility, low cost and nontoxicity [3–6]. Hematite, the most thermodynamically stable iron oxide phase, crystallizes in the rhombohedral morphology with a 2.1 eV bandgap [7] and hence absorb light in the visible range of the solar spectrum [8]. However, its

photoactivity is limited by the fast electron–hole pairs recombination [9]. Various approaches such as doping α -Fe₂O₃ with transition metals, which can overcome their limitations [10–12] have proposed. Therefore, coupling Fe₂O₃ with a semiconductor that has a lower conduction band (CB) edge would delay the recombination of the photoexcited electrons with the positive hole. Doping of various metal ions such as Mg²⁺, Cu²⁺, Ni²⁺, Ce⁺², and Zn²⁺ [13–15] at the Fe site in hematite influence the physical and photocatalytic properties. Where, the metal dopant serves as an ionized that likely improve the conductivity and the charge transport properties of the Fe₂O₃. The composite semiconductors generally possess a high photocatalytic activity as a result of their advantageous combined characteristics [16]. Numerous efforts have been made to improve the photocatalytic activity of both Fe₂O₃ and ZnO [17]. Particularly, spinel ferrites was intensively considered as photocatalysts due to its unique properties and high magnetism which facilitate the catalyst separation by applying an external magnetic field [18]. Likely, the ZnFe₂O₄ is a multi-active site with strong chemical stability. It also has a narrow bandgap (1.96 eV) which provide the advantageous photocatalysis in visible

✉ Radwa A. El-Salamony
radwa2005@hotmail.com

¹ Egyptian Petroleum Research Institute, 1A Ahmed El-Zomor St., Nasr City, Cairo 11727, Egypt



light range [19]. In addition, it is a cheap, ecofriendly, material with high thermal and mechanical strength and suitable for mass production [20]. ZnFe_2O_4 is intensively applied as sensitizer to influence the semiconductor photocatalytic activity in visible range as a result of its high sensitivity [21]. So that, ZnFe_2O_4 exhibited a high efficiency as photocatalyst for methyl orange and malachite green dyes mineralization [22]. Despite the ZnFe_2O_4 abundant benefits, its activity is dramatically affected by its morphology and structure.

NiFe_2O_4 is also an attractive semiconductor, due to its fabulous properties, that has been applied in many fields [23]. It is a promising photocatalyst in the visible range due to its small bandgap (2.19 eV) with a relative positioning conduction and valency bands and significant redox potential [24]. For example, NiFe_2O_4 exhibited a high photocatalytic activity of 98% in methyl orange mineralization in aqueous media at visible range light luminance [25]. Meanwhile, the pure NiFe_2O_4 as photocatalyst generally suffer a delayed electron excitation as well as fast electron/hole (e^-/h^+) recombination [26]. So that, combination of ferrites with other materials such as $\text{Bi}_{24}\text{O}_{31}\text{Br}_{10}$ [27] and zeolites [28] were investigated to overcome the ferrites disadvantages, increase the surface area and their electronic structure.

Very recently, the nickel ferrite has possessed a super reactivity as photocatalyst for elimination of complete decolorization of the colored water [29], elimination of antibiotics [30], heavy metals [31] from waste water. Zinc ferrite has also exhibited a wide spectrum of applications with superior efficiency toward waste water neutralization [32].

In this study, the NiFe_2O_4 and ZnFe_2O_4 as photocatalysts were synthesized by modified sol–gel method. The effects of the nickel and zinc oxides doping on the structural, morphological, and optical properties of their corresponding ferrite were investigated using several analytical techniques. The photocatalytic activities of the prepared catalysts were evaluated based on the degradation of amido black b10 dye in an aqueous solution under visible light.

2 Materials and Methods

2.1 Catalyst's Synthesis

The materials used in this work, the $\text{Fe}(\text{NO}_3)_3 \cdot 9\text{H}_2\text{O}$ (99.8%), $\text{Ni}(\text{NO}_3)_2 \cdot 6\text{H}_2\text{O}$ (99.9%) and $\text{Zn}(\text{NO}_3)_2 \cdot 6\text{H}_2\text{O}$ (99.9%), as an analytical grade were purchased from Sigma-Aldrich company. The supplied materials were used as obtained without any purifications. The pure $\alpha\text{-Fe}_2\text{O}_3$ was synthesized via modifying the method reported by Dong et al. [33]. Typically, a 2 M solution of $\text{Fe}(\text{NO}_3)_3 \cdot 9\text{H}_2\text{O}$ precursor was prepared. To the 2 M solution, 25% ethanol to water (v/v) was added and stirred for 1 h. The solution was then sonicated for 20 min to form solution 1. Part of the solution

was then dried under vigorous stirring at 80–120 °C. Finally, the powder was calcined under the airflow at 600 °C for 3 h. For the NiFe_2O_4 and ZnFe_2O_4 samples preparation, the calculated amount of nickel or zinc nitrates was dissolved in deionized water to form solution 2. Then, the previously prepared solution 1 were mixed with solution 2 in the presence of additional 20 ml ethanol until a clear solution mixture was obtained. The mixture was sonicated at 65 Hz power and 50% efficiency, later on it dried in overnight at 110 °C and calcined at 600 °C for 5 h.

2.2 Catalyst Characterization

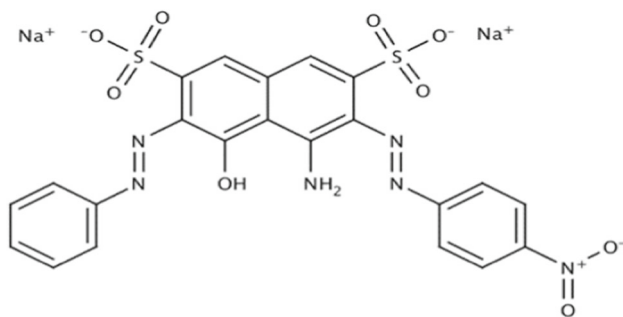
The formed crystalline phases and structure were investigated by the XRD analysis using the X'PertPRO PANalytical instrument. The apparatus equipped with a Ni filter with $K\alpha$ radiation ($\lambda = 0.15406$ nm). The lattice size of all the prepared samples was calculated according to Scherrer equation. The textural properties of the prepared catalysts were obtained by BET analysis using NOVA 3200 apparatus, USA, instrument. Before measurements, the catalysts were degassed at 120 °C for 3 h. The S_{BET} was calculated from the adsorption isotherm while pore size distributions (PSD) were calculated from desorption isotherms.

The sample morphologies were conducted by transmission electron microscope using the JOEL microscope (JEM-200CX, Japan) instrument worked at 200 kV. Before the analysis, the samples were suspended in ethanol and sonicated for 30 min. a few droplets were then placed on the copper grid and left to dry for 10 min then investigated. Fourier-transform infrared investigations were performed using Nicolet (Is-10 model, USA) spectrophotometer via the KBr technique. While, UV-reflectance was analyzed using a UV-spectrophotometer (V-570, JASCO, Tokyo, Japan). The direct bandgap energies for samples were estimated from the Tauc plot method via the following Equations:

$$(\alpha h\nu) = A(h\nu - E_g)^n \text{ where } \alpha = \frac{(1 - R)^2}{2R}$$

where E_g is the bandgap energy (eV), h is Planck's constant, $h\nu$ is the photon energy (eV), A is a proportional constant, and α is the absorption coefficient. The absorbance or Kubelka–Munk function of the reflectance ($f(R)$) is proportional to the absorption coefficient (α), and n is 0.5 and 2.0 for direct transition semiconductor and indirect transition semiconductor, respectively.

Photoluminescence (PL) analysis was measured at room temperature using the Spectrofluorometer model (JASCO FP-6500, Japan). ZetaSizer Nano Series (HT), Malvern Instruments UK, the instrument was used to determine the hydrodynamic particle size distribution of the prepared



Scheme 1 Chemical structure of Amido black 10 b dye

nanocomposite by dynamic light scattering technique in an aqueous solution medium.

2.3 Photocatalytic Activity

The amido black b10 azo dye ($C_{22}H_{14}N_6Na_2O_9S_2$) supplied by Fisher Scientific had the characteristics of molecular mass 616.487 g/mole; $\lambda_{max} = 584$ nm and pH 8. Scheme 1 represents the chemical structure of Amido black 10 b dye. All photocatalytic experiments were conducted in a cylindrical glass vessel with an air pump to continuously defuse the air through the suspension. The experiments were carried out with 1 g/L suspended photocatalyst/dye solution. Typically, 0.1 g catalyst suspended in a 100 ml aqueous solution of 25 mg/L Amido black b10 dye under three different pH of 4, 8, 10 were investigated. The experiments were performed under continuous stirring in the presence of 100W Tungsten visible lamp (> 400 nm). Before irradiation, the suspension was equilibrated under darkness for 30 min to reach the adsorption equilibrium. Aliquots of 2 mL were collected after interval times of illumination and then filtered through 0.22 mm filter. The filtrate was determined by a JENWAY-6505 UV–visible spectrophotometer at λ_{max} of 584 nm.

3 Results and Discussion

3.1 XRD Analysis

The samples crystallography and patterns are investigated by XRD and illustrated in Fig. 1. The pure iron oxide sample (Fig. 1a) showed 2θ of 24.05° , 32.94° , 35.53° which are the main characteristic peaks of the (012), (104), (110) plans of rhombohedral hematite α - Fe_2O_3 structure [34, 35]. The recorded peaks have well-defined positions with high sharpness and intensity that implies the prepared samples high crystallinity. In addition, the absence of any other patterns corresponding to other iron oxide phases reflects the sample high purity.

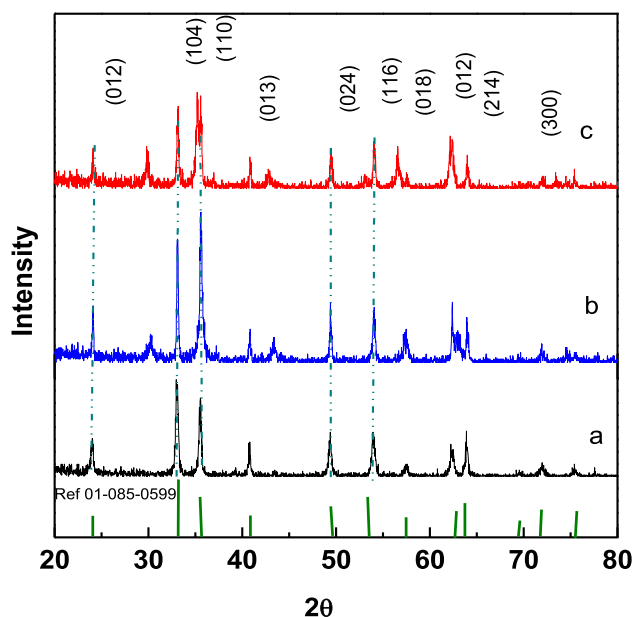


Fig. 1 The XRD pattern of the a α - Fe_2O_3 , b $NiFe_2O_4$ and c) $ZnFe_2O_4$ samples

The $NiFe_2O_4$ diffractogram (Fig. 1b) showed all the pure α - Fe_2O_3 peaks with relatively high intensity and sharpness compared with the pure α - Fe_2O_3 . The sharp peak at 35.51° accompanied with small patterns at 2θ of 30.3° , 43.37° , 57.37° , 63.2° assigned to (220), (311), (400), (511), and (440) crystal planes of the $NiFe_2O_4$ spinel form [36].

The XRD analysis of the $ZnFe_2O_4$ sample (Fig. 1c) demonstrated the α - Fe_2O_3 characteristic peaks exhibited much lower intensities than the pure hematite sample. Moreover, all the recorded peaks to the $ZnFe_2O_4$ sample had an obvious broadening which reflects a smaller particle size. The sample was showed a distinguishable diffraction peak at 2θ of 30.0° , 35.2° , 35.6° , and tiny peaks at 42.78° , 53.06° and 73.38° corresponding to (220), (311), (222), (400), (440) and (533) of plane for cubic $ZnFe_2O_4$ lattice [37] All the recorded peaks are in good agreement with the standard JCPDS card no. 22-1012 [38].

The average crystallite size was calculated using the Debye–Scherrer equation [39] via the FWHM of the main peaks corresponds to (104) and (311) planes of the pure α - Fe_2O_3 , $ZnFe_2O_4$, respectively. The obtained results are represented in Table 1. The table indicates the pure α - Fe_2O_3 small size of about 29 nm. Meanwhile, the α - Fe_2O_3 crystallite was enlarged by almost two folds when by Ni doping while slightly increased in the case of Zn doped hematite. The lattice enlargement may be explained via the undistributed cations, where Fe^{3+} is allocated in a large octahedral structure while the Ni^{2+} or Zn^{2+} is located in a small tetrahedral shape as in the normal case of the bulk ferrite materials formation at high temperature [40, 41]. This observation indicated that the

Table 1 The calculated crystallite size of the prepared samples

Sample	Crystallite size of formed Phases								
	Fe ₂ O ₃			NiFe ₂ O ₄			ZnFe ₂ O ₄		
	2θ	FWHM	D (nm)	2θ	FWHM	D (nm)	2θ	FWHM	D (nm)
α-Fe ₂ O ₃	32.94	0.3149	29.7	–	–	–	–	–	–
NiFe ₂ O ₄	33.07	0.1771	52.9	35.51	0.1181	81.7	–	–	–
ZnFe ₂ O ₄	33.14	0.2362	39.7	–	–	–	35.21	0.1968	48

NiFe₂O₄ and ZnFe₂O₄ had formed in regular lattice structures without any distortion. The much smaller lattice size in the ZnFe₂O₄ sample than NiFe₂O₄ related to the large ionic radius of Zn²⁺ (0.84 Å) as compared to the ionic radius of Ni³⁺ (0.74 Å).

3.2 BET Results

The N₂ adsorption–desorption isotherms and particle size distribution curves are measured to determine the catalysts textural properties and illustrated in Fig. 2A, B, respectively. Figure 2A clearly indicates that all samples exhibited BET isotherms of Type IV according to IUPAC classification [42]. Furthermore, all samples' isotherms had hysteresis loops but in a different manner. Whereas, the pure Fe₂O₃ and ZnFe₂O₄ samples exhibited an H4 hysteresis loop according to the IUPAC system which indicated the presence of mixed pore structure [43]. Meanwhile, For the NiFe₂O₄ sample, the H3 hysteresis loop was obtained [44]. This hysteresis type normally belongs to the ink bottle flexible aggregates with plate-like has given rise to slit-shaped pores. Also, the hysteresis indicated the ink bottle with a wide neck and small volume-shaped pores. The obtained isotherms imply the existence of pores within the mesoporous range in all samples. For all the prepared samples, the presence of the isotherm

plateau in desorption curve for the H3 hysteresis loops confirms the presence of large mesopores in the sample.

The pore size distribution (PSD) (Fig. 2B-a) indicated that the pure Fe₂O₃ sample has a smooth PSD curve ranged in a large mesoporous range of 15–45 nm which centered around 22 nm. The pore size distribution of the NiFe₂O₄ sample (Fig. 2B-b) demonstrated a closure PSD while its curve allocated at a moderate mesoporous range of 10–35 nm with an average pore size of 16.5 nm. The detected smaller pore size of NiFe₂O₄ sample fitted the indicated different hysteresis loops for both samples. Also, this result indicated the possible incorporation of NiO particles into the Fe₂O₃ pores and narrowing it to lower pore size. This result explains further the obtained XRD results of tiny NiO peaks. The ZnFe₂O₄ sample (Fig. 2B-c) has shown bimodal pore size distribution located at microporous range of 2–6 and mesopores in range of 10–45 nm with average pore size of 22.6 nm. This observation can be explained via the ZnO partial incorporation into the large ranged Fe₂O₃ mesopores.

Table 2 shows that all samples were characterized by small S_{BET} of 26.2, 31.4, and 25.8 m²/g while pore volume was 0.097, 0.115, and 0.196 for α-Fe₂O₃, NiFe₂O₄ and ZnFe₂O₄ samples, respectively. The table demonstrated a slight increase in surface area with low particle size for NiFe₂O₄ sample. This can be explained by the formation of

Fig. 2 The N₂ adsorption–desorption isotherms (A) and PSD curves (B) of (a) Fe₂O₃, (b) NiFe₂O₄ and (c) ZnFe₂O₄

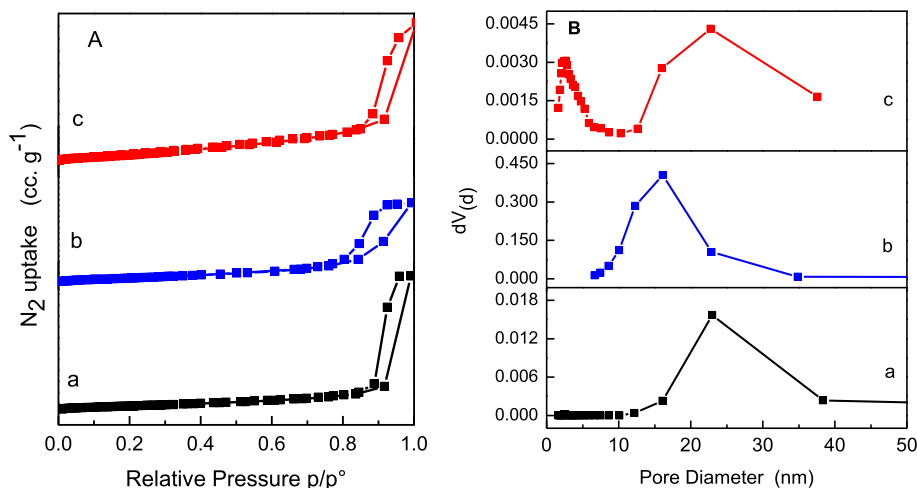
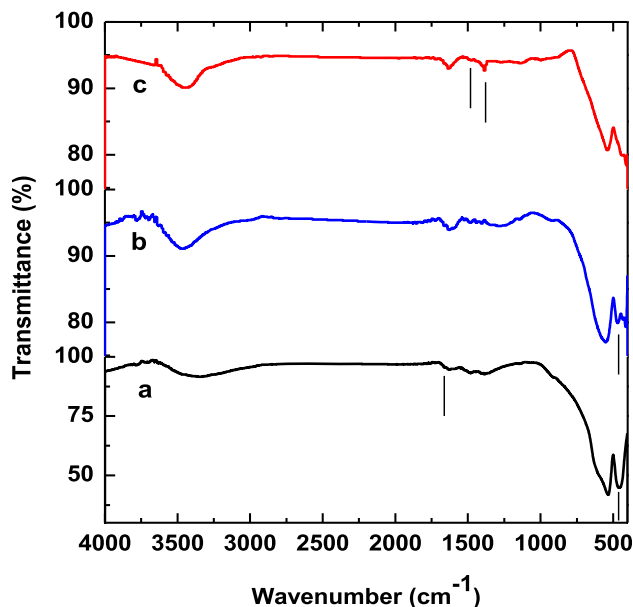


Table 2 The surface area, textural properties and bandgap energy of the prepared samples

Catalyst	S_{BET} (m^2/g)	V_p (cm^3/g)	r_p (nm)	D_{BET}	Indirect bandgap energy (eV)	direct bandgap energy (eV)
$\alpha\text{-Fe}_2\text{O}_3$	26.2	0.196	22.9	43.8	1.9	1.92
NiFe_2O_4	31.4	0.115	16.5	36.4	3.1	1.9
ZnFe_2O_4	25.8	0.097	22.6	44.3	2	2

**Fig. 3** FTIR spectra of **a** $\alpha\text{-Fe}_2\text{O}_3$, **b** NiFe_2O_4 , and **c** ZnFe_2O_4 , separate lines indicate the peaks difference between samples

NiO small particles onto the Fe_2O_3 surface. While loading of ZnO resulted in decreasing the surface area and particle size. In conclusion, companying the BET with the XRD results confirms the synthesis of NiFe_2O_4 accompanied with some additional surface small NiO particles. Meanwhile, other particles were introduced to the Fe_2O_3 pores and cause pores neck widening as indicated from the BET calculations. On the other hand, the absence of ZnO patterns in XRD along with small pore volume and particle size indicated that Zn ions had mostly involved in the ZnFe_2O_4 framework formation.

3.3 FTIR Results

The FTIR spectrum of pure Fe_2O_3 (Fig. 3a) showed two closer intense peaks around 458.7, 550 cm^{-1} and a small peak at 1621 cm^{-1} . Those recorded peaks attributed to the stretching vibration of the tetrahedral Fe-O group in Fe_2O_3 nanoparticles [45, 46]. The spectrum of NiFe_2O_4 (Fig. 3b) has shown an additional intense peak at 420 cm^{-1} which ascribed to the Ni-O stretching vibration. Also, a small shoulder at 846 cm^{-1} and a wide peak at 1380 cm^{-1} assigned

to the stretching vibration in metal-O bond in a tetrahedral structure. The detected peaks have confirmed the NiO and Fe_2O_3 coexistence and also the formation of NiFe_2O_4 spinel form which runs with the XRD results (see Fig. 1b). Figure 3c shows peaks at 446 and 539 cm^{-1} which belonged to the stretching vibration of Zn-O and Fe-O , respectively. Whereas, no other peaks assigned to the ZnO were observed. These results indicated the formation of the ZnFe_2O_4 spinel with some pure Fe_2O_3 nanoparticles [47]. Furthermore, all samples had wide broad peaks at 3345.6, 3465.1, and 3432.2 cm^{-1} ascribed to either the $-\text{OH}$ stretching vibration of the free adsorbed water molecules and/or the superficial $-\text{OH}$ group of the metal oxide. Generally, the observed shift in metal oxides characteristic peaks to a lower wave number revealed their electronic structure interaction.

3.4 TEM Analysis

The electron microscope image of $\alpha\text{-Fe}_2\text{O}_3$ sample (Fig. 4a) revealed the dominant formation of regular crystalline rhombohedral structure. The figure also revealed a small nanoscale particle with narrow particle size distribution in a range of 26–35 nm and slight agglomeration degree. NiFe_2O_4 micrograph (Fig. 4b) showed the formation of some large and irregular hexagonal-shaped particles accompanied with penalty of irregular cubic-shaped small particles. The large existed particles in Fig. 4b had an average particle size of 70 nm while the cubic small particles had particle size distribution ranged from 14 to 18 nm.

The ZnFe_2O_4 sample (Fig. 4c) was assembled by a much smaller particle size and much aggregates tiny amount than the NiFe_2O_4 sample. The figure demonstrated the irregular shape fabricated ZnFe_2O_4 particles. It is worth to mention that the observed porosity in electron microscope images can be due to the formed particles inter distance raised by evaporation of organic solvent during calcination. The observed porous nature that would enhances the photocatalytic activity are in good agreement with the X-ray diffraction and surface area results.

3.5 Zeta Potential

The behavior of nanoparticles and their efficiency to decline the dispersion rate of stable and durable very small particles

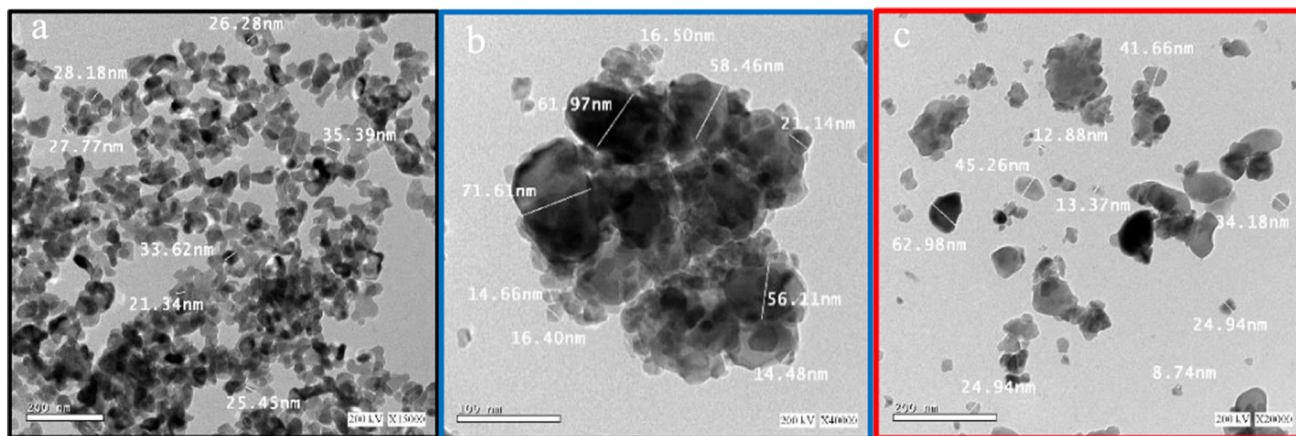


Fig. 4 The TEM images of samples **a** α -Fe₂O₃, **b** NiFe₂O₄, and **c** ZnFe₂O₄

in aqueous solutions is highly affected by the zeta potential values. Where the repulsion rate between the similar and/or neighbor particles in aquatic solution is normally decided by zeta potential property. The dispersed tiny particles generally need a high zeta potential value to form a stable solution. While the particles with low zeta potential tend to accumulate and form large masses [48, 49]. On the other hand, very stable suspended particles, which have a zeta potential of ± 30 mV, creates an electrostatic divergence between particles and prevent accumulation [49]. Measuring the zeta potentials at different pH values provides the nanoparticles isoelectric point pH_{pzc} . The pH_{pzc} is effectively determined the pH value whereas the adsorbent can adsorb both negatively or positively charged particles. When the pH of the solution is less than pH_{pzc} , the surface charge of the adsorbent is positive, while its surface charge is negative when the pH of the solution is greater than pH_{pzc} [50].

In this work, the zeta potentials of the prepared catalysts were measured in water to determine their isoelectric point and the results are illustrated in Fig. 5. The Figure showed that the obtained pH_{pzc} values were 5.01, 5.31, and 5.62 for the NiFe₂O₄, Fe₂O₃, and ZnFe₂O₄ samples respectively. The obtained pH_{pzc} value of the ZnFe₂O₄ in this work is slightly lower than the result reported in Ref. [51] which indicates the positive load in the Zinc ferrite structure. Since the Amido 10b molecules are negatively charged and the ZnFe₂O₄ surface positive load, higher dye absorptivity and hence the higher photocatalytic degradation would be achieved. Depending on the surface area data and the obtained pH_{pzc} values, it is expected that the ZnFe₂O₄ sample would possess a higher photocatalytic activity.

3.6 Optical Properties

The optical properties of the prepared photocatalysts were studied by UV–visible diffuse reflectance spectroscopy and

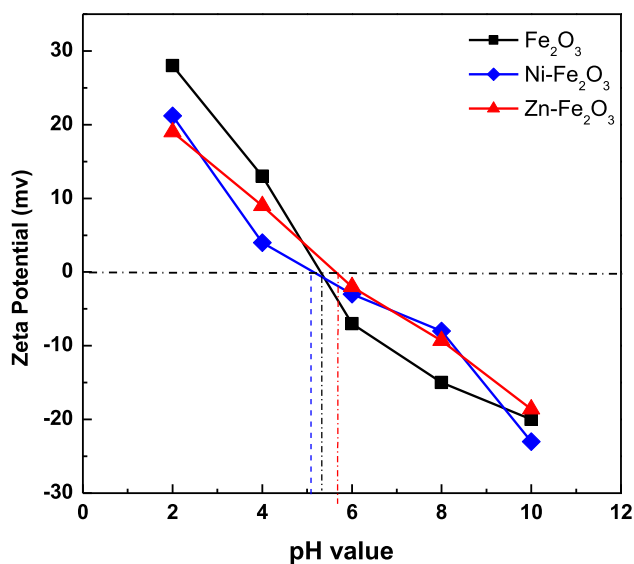


Fig. 5 Zeta potential measurements of the α -Fe₂O₃, NiFe₂O₄, and ZnFe₂O₄ samples in water as solvent

PL. Figure 6 shows the UV–vis diffuse reflectance spectra of pure α -Fe₂O₃, NiFe₂O₄, and ZnFe₂O₄ samples. All samples exhibit the absorption band in 347 nm results from the ligand to metal charge transfer transition (direct transition) [52], a broad absorption in the measured region (350–600 nm) and a characteristic bandgap absorption edge of α -Fe₂O₃ at 550 nm [53]. The absorption edge of α -Fe₂O₃, NiFe₂O₄ samples are identical, however; the absorption edge of the ZnFe₂O₄ sample shifts to the visible range and has a low absorption intensity than Fe₂O₃ as a result of electronic interactions between Fe₂O₃ and ZnO indicating the ZnFe₂O₄ spinel form; as represented in XRD.

The indirect and a direct bandgap were indicated from Tauc plots that showed in Fig. 7, while the bandgap energy is given in Table 2. Authors in [54] have reported that α -Fe₂O₃ has an indirect bandgap. The indirect bandgap values

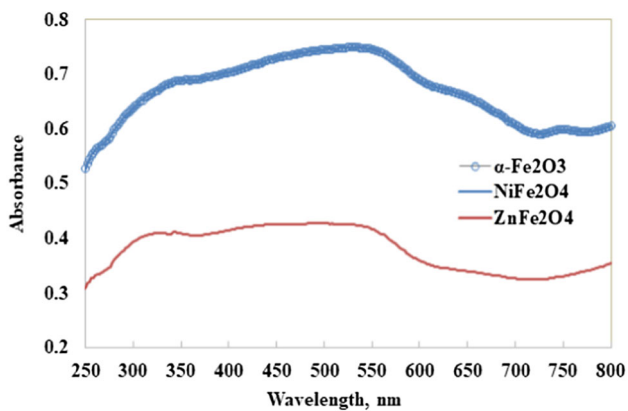


Fig. 6 The absorption spectrum of the prepared samples in UV to near IR regions of **a** $\alpha\text{-Fe}_2\text{O}_3$, **b** NiFe_2O_4 and **c** ZnFe_2O_4 samples

were reported within the range of 1.38–2.09 eV [55, 56]. While, the direct bandgap between 1.95 and 2.35 eV can be distinguished [57]. The Fe^{3+} absorption in the visible region

is generally attributed to the 3d–3d spin forbidden transition excitation (indirect transition). Where, the direct bandgap of $\alpha\text{-Fe}_2\text{O}_3$ is about 1.8 eV, which is consistent with reported literature [58]. Herein, the observed bandgap energy of the sample has a direct bandgap occurring in conjunction with an indirect bandgap [59].

The indirect bandgap of $\alpha\text{-Fe}_2\text{O}_3$ is 1.9, in agreement with the typical literature value from 1.9–2.2 eV, depending on the crystalline status and methods of preparation [60]. As in NiFe_2O_4 , the bandgap obtained from the indirect gap is 1.9–3.1 eV and that from direct bandgap is 1.92–1.9 eV. The slightly reduce in direct bandgap is attributed to the slightly affected conduction band edge of $\alpha\text{-Fe}_2\text{O}_3$ by the incorporation of nickel in the lattice [61]. This result confirms the formation of NiFe_2O_4 spinel ferrite as indicated from the XRD and FTIR analysis. In the case of ZnFe_2O_4 catalyst, the obtained indirect bandgap is 1.9–2 eV and the determined direct bandgap is 1.92–2 eV. The increase in bandgap energy usually occurred in case of higher loaded percent of Ni [62],

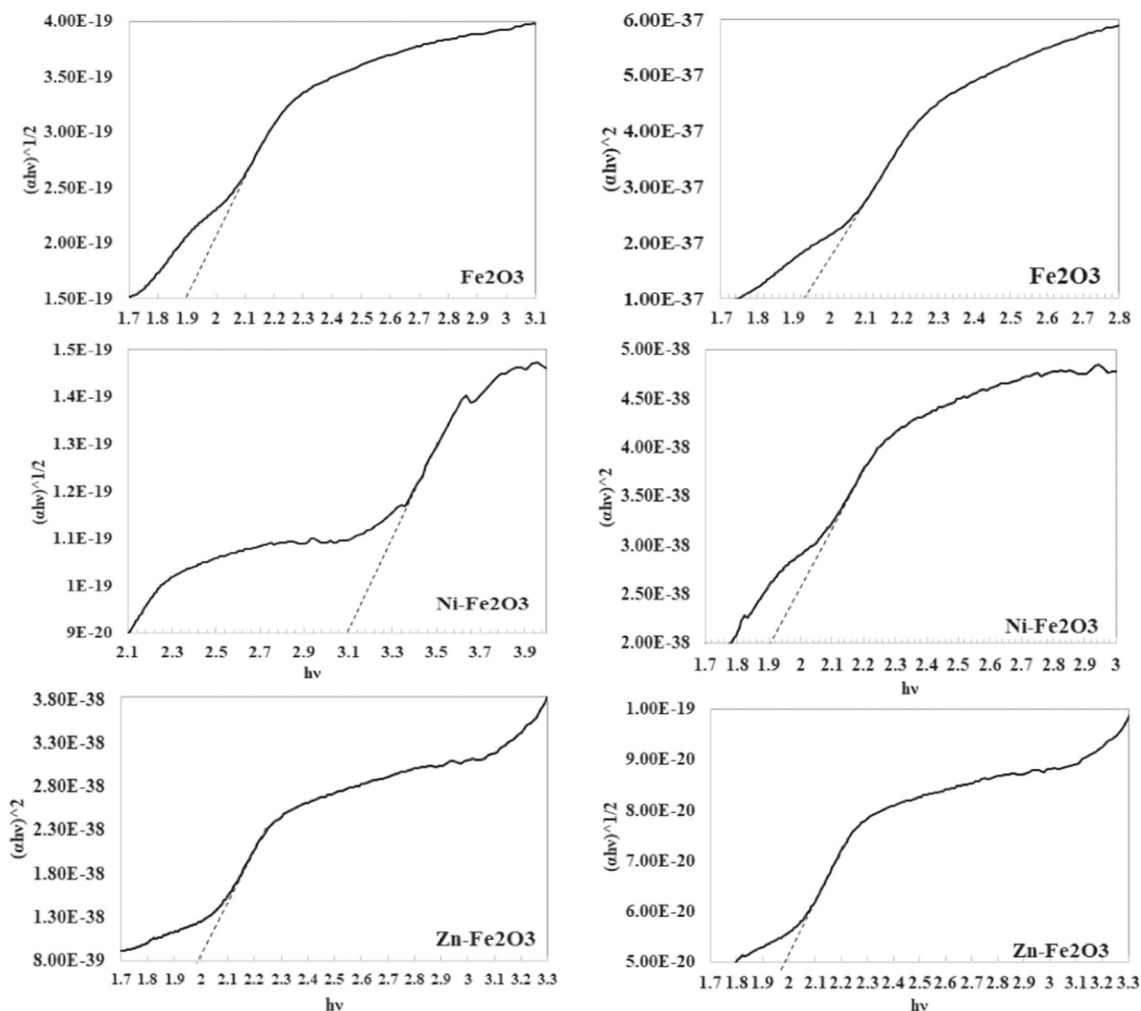


Fig. 7 Tauc plots for an indirect transition, and direct transition $(\alpha h\nu)^2$ versus $(h\nu)$ of $\alpha\text{-Fe}_2\text{O}_3$, NiFe_2O_4 , and ZnFe_2O_4 samples

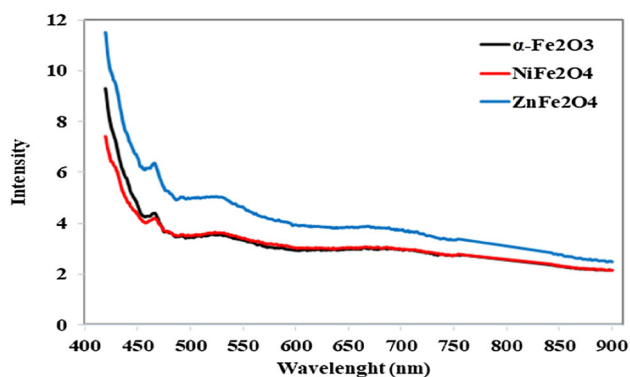


Fig. 8 PL spectra of the prepared photocatalysts under 400 nm for the prepared samples

Zn [63], and Ho [64] more than in this work. This confirms the much higher surface Ni than in bulk; as represented in the results of transmission electron microscope and surface area analysis. This behavior of NiO is in-line with results reported by Liu [34]. In general; the results suggest that electron/hole pairs can be generated, although the particle is illuminated with long wavelength visible light.

The trapping efficiency, migration, and charge carriers transfer are important factors that generally determined from the photoluminescence technique. However; the intensity of the photoluminescence spectrum is directly proportional with the electron–hole recombination rate [63]. Photoluminescence characterization under a wavelength excitation of 400 nm, corresponding to the visible light used in the photodegradation experiment, is shown in Fig. 8. The pure α -Fe₂O₃, NiFe₂O₄, and ZnFe₂O₄ samples showed the same photoluminescence emission at 468, 534, and 688 nm. The PL intensity of the α -Fe₂O₃ sample is identical to NiFe₂O₄ but the PL intensity of the ZnFe₂O₄ sample again; these results indicated the formation of the ZnFe₂O₄ spinal form.

3.7 Photocatalytic Activity

Photodegradation of amido black 10B dye was carried out using α -Fe₂O₃, NiFe₂O₄, and ZnFe₂O₄ photocatalysts under visible light at different pH 4, 8, and 10 for 90 min; as shown in Fig. 9. Initially, the experiment was conducted in dark for 30 min to reach the adsorption/desorption equilibrium before catalyst illumination. In all cases; the photodegradation is in parallel with the adsorption affinity of the photocatalysts and the doped metal increased the adsorption capacity of Fe₂O₃. Photocatalytic activity is maximum for natural dye pH 8, good for pH 4, and minimum for pH 10 as shown in Fig. 9.

At pH 4, Amido black 10b dye photodegradation was 91%, 88.3%, and 88% for ZnFe₂O₄, Fe₂O₃, and NiFe₂O₄ photocatalysts, respectively. This result is matching the zeta potential value of the photocatalysts; whereas; the catalyst

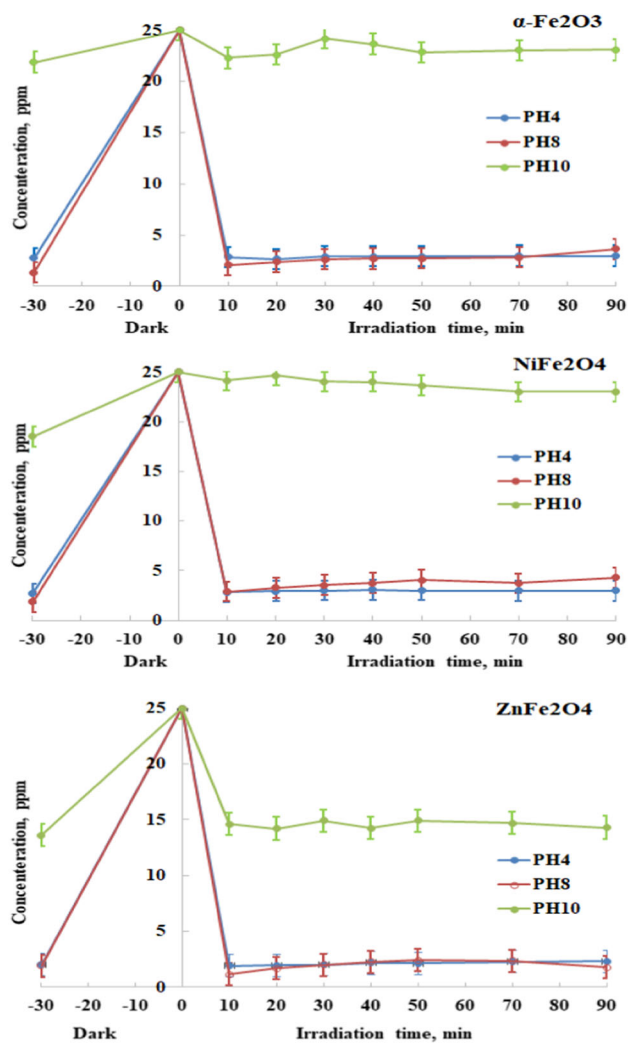
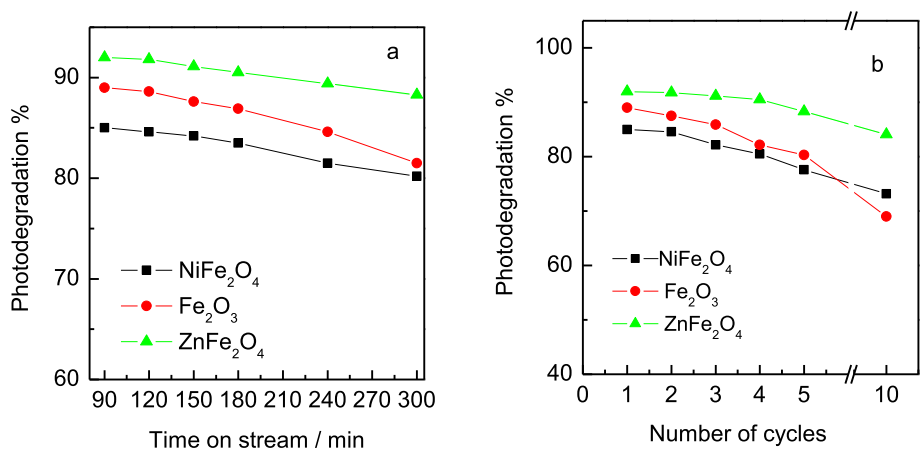


Fig. 9 Photoactivity of the α -Fe₂O₃, NiFe₂O₄, and ZnFe₂O₄ samples toward the degradation of Amido black b10 dye using 1 g/L of catalyst, at three different pH under visible light

exhibited the highest zeta potential to increase the dispersion and stability of the catalyst particles in water and charge transfer which effective positively on adsorption and photocatalytic activity [65]. The electrostatic interaction of dye molecules with a positively charged catalyst particle surface may be the cause of the photocatalytic performance at pH 4 [66].

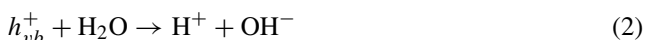
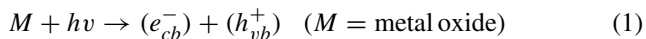
At pH 8; the photodegradation of dye has reached the maximum of 92%, 89%, and 85% for ZnFe₂O₄, α -Fe₂O₃ and NiFe₂O₄ photocatalysts; respectively. The highest photoactivity of ZnFe₂O₄ sample can also attributed to the low bandgap of 2 eV in comparison to 3 eV assigned to NiFe₂O₄ photocatalyst. The creation of superficial ⁻OH group in ZnFe₂O₄, as confirmed by FTIR, is crucial property. Since, ⁻OH can react with the photoexcited holes originated on the catalyst surface, producing hydroxyl radicals, that acts as powerful oxidants.

Fig. 10 The catalysts **a** durability and **b** reusability toward the Amido black b10 dye photodegradation



In general, in a neutral medium; when the photocatalysts are exposed to visible light the electron transfer takes place from valance band to conduction band (e_{cb}^-) and a hole is created in the valance band (h_{vb}^+). Hydroxyl ions combine with a positive hole to produce $\cdot\text{OH}$. Thus, $\cdot\text{OH}$ radical is attacking the double bond in the dye molecules which resulting its mineralization [67].

The oxygen present in the dye solution functions as an electron scavenger. This oxygen traps the electrons from the conduction band and forms superoxide radical anion $\text{O}_2^{\cdot-}$ species. This prevents the recombination of positive holes in the valance band and the electrons in the conduction band. Further $\text{O}_2^{\cdot-}$ is reacting with chemisorbed H^+ on conduction band to produce peroxide radicals HO_2^{\cdot} active radical as illustrated in Eqs. 1–5 Scheme 2.



The Amido black 10b dye photodegradation is negligible in the case of Fe_2O_3 , and NiFe_2O_4 catalysts at pH 10, due to the electrostatic repulsion between negatively charged catalyst surface and dye ions [66] at high basic medium. While, in case of ZnFe_2O_4 , the photodegradation reached only 40%.

The durability of the three catalysts was studied under the determined optimum conditions along 5 h. During the study, an aliquot was firstly collected each 30 min for 3 h. Then a liquid sample was separated every one hour for further 2 h. The results in Fig. 10a imply that the loss in photodegradation affinity was 8%, 5% and 3% over the Fe_2O_3 , NiFe_2O_4

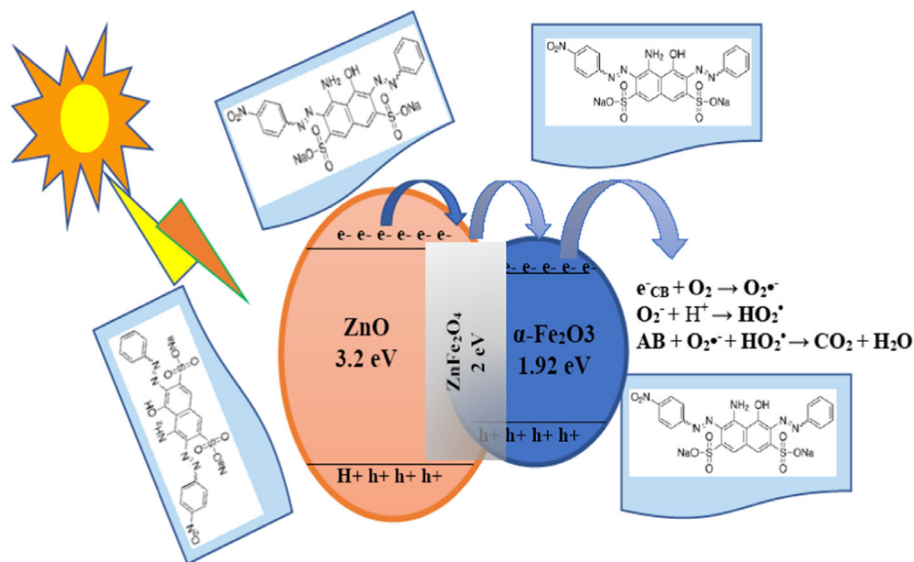
and ZnFe_2O_4 , respectively. These observations prove the catalysts super durability for Amido black 10b dye removal.

For more convenience, the catalysts reusability were investigated along 10 reaction cycles. Figure 10b shows that catalytic activity along the investigated cycles were in order of $\text{ZnFe}_2\text{O}_4 > \text{NiFe}_2\text{O}_4 > \text{Fe}_2\text{O}_3$. Meanwhile the decreasing in activity profile of Fe_2O_3 was faster than the other two catalysts. The photodegradation was decreased by 8%, 12% and 21% over the ZnFe_2O_4 , NiFe_2O_4 and Fe_2O_3 , respectively.

4 Conclusion

In this study, the photocatalytic performance of the NiFe_2O_4 and ZnFe_2O_4 catalysts toward the Amido black b10 dye removal was investigated. The NiFe_2O_4 and ZnFe_2O_4 samples were prepared by the modify sol–gel method. The X-ray diffraction results showed the main characteristic peaks of rhombohedral pure Fe_2O_3 in all prepared samples. The results also confirmed the formation of ferrite structure in samples while the diffractograms showed none of the NiO or ZnO main peaks. The Fe_2O_3 lattice size was slightly increased in the ZnFe_2O_4 sample and enlarged by NiO doping. Surface analyses have confirmed the synthesis of mesoporous structure with relatively low surface area and moderate mesopore size samples. Meanwhile, the ZnFe_2O_4 sample exhibited mixed low and moderate-size mesopores. The NiFe_2O_4 showed a considerable S_{BET} value more than $\alpha\text{-Fe}_2\text{O}_3$ and ZnFe_2O_4 samples. The transmission electron microscope showed no rhombohedral structure in the NiFe_2O_4 and ZnFe_2O_4 samples. Where segregated small particles may attribute to the NiO in the NiFe_2O_4 sample was observed. This result revealed the uncompleted incorporation of NiO into the ferrite structure. While no ZnO particles were observed in ZnFe_2O_4 samples which confirmed the successive ferrite structure synthesis. The Ferrier transition infrared results indicated the existence of assigned pure NiO

Scheme 2 A proposed visible light photodegradation mechanism of ZnFe₂O₄ sample at pH 8



which confirms the NiO small clusters formation in the sample. As the Ni doping in NiFe₂O₄, the bandgap obtained from the indirect gap is 1.9–3.1 eV, whereas; in the case of ZnFe₂O₄ catalyst the bandgap obtained from the indirect gap is 1.9–2 eV. The photodegradation toward Amido black b10 dye is reached maximum value under visible light at natural dye pH 8, and it reaches 92%, 89%, and 85% over ZnFe₂O₄, Fe₂O₃, and NiFe₂O₄ photocatalysts; respectively.

Acknowledgements This work was supported by the labs of the Egyptian Petroleum Research Institute (EPRI).

Funding Open access funding provided by The Science, Technology & Innovation Funding Authority (STDF) in cooperation with The Egyptian Knowledge Bank (EKB). This research did not receive any specific grant from funding agencies in the public, commercial, or not-for-profit sectors. This work was supported by the laboratories of the Egyptian Petroleum Research Institute (EPRI).

Data Availability The original data will be available upon request to the corresponding author.

Declarations

Conflict of interest The authors declare that they have no competing interests.

Open Access This article is licensed under a Creative Commons Attribution 4.0 International License, which permits use, sharing, adaptation, distribution and reproduction in any medium or format, as long as you give appropriate credit to the original author(s) and the source, provide a link to the Creative Commons licence, and indicate if changes were made. The images or other third party material in this article are included in the article's Creative Commons licence, unless indicated otherwise in a credit line to the material. If material is not included in the article's Creative Commons licence and your intended use is not permitted by statutory regulation or exceeds the

permitted use, you will need to obtain permission directly from the copyright holder. To view a copy of this licence, visit <http://creativecommons.org/licenses/by/4.0/>.

References

- Su, F.; Li, P.; Huang, J.; Gu, M.; Liu, Z.; Xu, Y.: Photocatalytic degradation of organic dye and tetracycline by ternary Ag₂O/AgBr-CeO₂ photocatalyst under visible-light irradiation. *Sci. Rep.* **11**, 1–13 (2021)
- Bouarroudj, T.; Aoudjit, L.; Djahida, L.; Zaidi, B.; Ouraghi, M.; Zioui, D.; Mahidine, S.; Shekhar, C.; Bachari, K.: Photodegradation of tartrazine dye favored by natural sunlight on pure and (Ce, Ag) co-doped ZnO catalysts. *Water Sci. Technol.* **83**, 2118–2134 (2021)
- Mor, G.K.; Prakasam, H.E.; Varghese, O.K.; Shankar, K.; Grimes, C.A.: Vertically oriented Ti-FeO nanotube array films: toward a useful material architecture for solar spectrum water photoelectrolysis. *Nano Lett.* **7**, 2356–2364 (2007)
- El-Sheikh, S.M.; Harraz, F.A.; Abdel-Halim, K.S.: Catalytic performance of nanostructured iron oxides synthesized by thermal decomposition technique. *J. Alloys Compd.* **487**, 716–723 (2009)
- Chahal, S.; Kumar, A.; Kumar, P.: Zn doped α-Fe₂O₃: an efficient material for UV driven photocatalysis and electrical conductivity. *Crystals* **10**, 273 (2020)
- Bagheri, S.; Chandrappa, K.; Hamid, S.B.A.: Generation of hematite nanoparticles via sol-gel method. *Res. J. Chem. Sci.* ISSN 2013, 2231, 606X
- Teja, A.S.; Koh, P.-Y.: Synthesis, properties, and applications of magnetic iron oxide nanoparticles. *Prog. Cryst. Growth Charact. Mater.* **55**, 22–45 (2009)
- Lin, Y.; Yuan, G.; Sheehan, S.; Zhou, S.; Wang, D.: Hematite-based solar water splitting: challenges and opportunities. *Energy Environ. Sci.* **4**, 4862–4869 (2011)
- Franking, R.; Li, L.; Lukowski, M.A.; Meng, F.; Tan, Y.; Hamers, R.J.; Jin, S.: Facile post-growth doping of nanostructured hematite photoanodes for enhanced photoelectrochemical water oxidation. *Energy Environ. I Sci.* **6**, 500–512 (2013)
- Liang, H.; Jiang, X.; Chen, W.; Wang, S.; Xu, B.; Wang, Z.: α-Fe₂O₃/Pt hybrid nanorings and their enhanced photocatalytic activities. *Ceram. Int.* **40**, 5653–5658 (2014)



11. Wu, R.-A.; Lin, C.W.; Tseng, W.J.: Preparation of electrospun Cu-doped α -Fe₂O₃ semiconductor nanofibers for NO₂ gas sensor. *Ceram. Int.* **43**, S535–S540 (2017)
12. Ctibor, P.; Pala, Z.; Stengl, V.; Musalek, R.: Photocatalytic activity of visible-light-active iron-doped coatings prepared by plasma spraying. *Ceram. Int.* **40**, 2365–2372 (2014)
13. Ingler, W.B., Jr.; Baltrus, J.P.; Khan, S.U.M.: Photoresponse of p-type zinc-doped iron (III) oxide thin films. *J. Am. Chem. Soc.* **126**, 10238–10239 (2004)
14. Ingler, W.B., Jr.; Khan, S.U.M.: Photoresponse of spray pyrolytically synthesized copper-doped p-Fe₂O₃ thin film electrodes in water splitting. *Int. J. Hydrog. Energy* **30**, 821–827 (2005)
15. Suman, P.K.; Chahal, S.; Kumar, A.; Kumar, P.: Zn doped α -Fe₂O₃: an efficient material for UV driven photocatalysis and electrical conductivity. *Crystals* **10**, 273 (2020)
16. Hernández, A.; Maya, L.; Sánchez-Mora, E.; Sánchez, E.M.: Sol-gel synthesis, characterization and photocatalytic activity of mixed oxide ZnO-Fe₂O₃. *J. Solgel Sci. Technol.* **42**, 71–78 (2007)
17. Uma, K.; KrishnaKumar, B.; Pan, G.-T.; Yang, T.C.K.; Lin, J.-H.: Enriched silver plasmon resonance activity on the sonochemical synthesis of ZnO flowers with α -Fe₂O₃ as an efficient catalyst for photo-Fenton reaction and photo-oxidation of ethanol. *J. Water Process Eng.* **34**, 101089 (2020)
18. Singh, P.; Gautam, S.; Shandilya, P.; Priya, B.; Singh, V.P.; Raizada, P.: Graphene bentonite supported ZnFe₂O₄ as superparamagnetic photocatalyst for antibiotic degradation. *Adv. Mater. Lett.* **8**, 10 (2017)
19. Khurshid, R.; Ali, F.; Afzal, A.; Ali, Z.; Qureshi, M.T.: Polyol-mediated coprecipitation and aminosilane grafting of superparamagnetic, spinel ZnFe₂O₄ nanoparticles for room-temperature ethanol sensors. *J. Electrochem. Soc.* **166**, B258 (2019)
20. Chen, C.-H.; Liang, Y.-H.; Zhang, W.-D.: ZnFe₂O₄/MWCNTs composite with enhanced photocatalytic activity under visible-light irradiation. *J. Alloy. Compd.* **501**, 168–172 (2010)
21. Zhang, L.; He, Y.; Ye, P.; Wu, Y.; Wu, T.: Visible light photocatalytic activities of ZnFe₂O₄ loaded by Ag₃VO₄ heterojunction composites. *J. Alloys Compd.* **549**, 105–113 (2013)
22. Chandel, N.; Sharma, K.; Sudhaik, A.; Raizada, P.; Hosseini-Bandegharai, A.; Thakur, V.K.; Singh, P.: Magnetically separable ZnO/ZnFe₂O₄ and ZnO/CoFe₂O₄ photocatalysts supported onto nitrogen doped graphene for photocatalytic degradation of toxic dyes. *Arab. J. Chem.* **13**, 4324–4340 (2020)
23. Kiani, F.; Naeimi, H.: Ultrasonic accelerated coupling reaction using magnetically recyclable bis (propyl molononitril) Ni complex nanocatalyst: a novel, green and efficient synthesis of biphenyl derivatives. *Ultrason. Sonochem.* **48**, 267–274 (2018)
24. Younas, M.; Nadeem, M.; Atif, M.; Grossinger, R.: Metal-semiconductor transition in NiFe₂O₄ nanoparticles due to reverse cationic distribution by impedance spectroscopy. *J. Appl. Phys.* **109**, 093704 (2011)
25. Xu, S.H.; Feng, D.L.; Li, D.X.; Shanguan, W.F.: Preparation of magnetic photocatalyst TiO₂ supported on NiFe₂O₄ and effect of magnetic carrier on photocatalytic activity. *Chin. J. Chem.* **26**, 842–846 (2008)
26. Gautam, S.; Shandilya, P.; Singh, V.P.; Raizada, P.; Singh, P.: Solar photocatalytic mineralization of antibiotics using magnetically separable NiFe₂O₄ supported onto graphene sand composite and bentonite. *J. Water Process Eng.* **14**, 86–100 (2016)
27. He, Z.; Xia, Y.; Su, J.; Tang, B.: Fabrication of magnetically separable NiFe₂O₄/Bi₂₄O₃₁Br₁₀ nanocomposites and excellent photocatalytic performance under visible light irradiation. *Opt. Mater.* **88**, 195–203 (2019)
28. Davari, N.; Farhadian, M.; Nazar, A.R.S.; Homayoonfal, M.: Degradation of diphenhydramine by the photocatalysts of ZnO/Fe₂O₃ and TiO₂/Fe₂O₃ based on clinoptilolite: structural and operational comparison. *J. Environ. Chem. Eng.* **5**, 5707–5720 (2017)
29. Bayantong, A.R.B.; Shih, Y.-J.; Dong, C.-D.; Garcia-Segura, S.; de Luna, M.D.G.: Nickel ferrite nanoenabled graphene oxide (NiFe₂O₄@GO) as photoactive nanocomposites for water treatment. *Environ. Sci. Pollut. Res.* **28**, 5472–5481 (2021)
30. Wang, Z.; Zhang, X.; Zhang, H.; Zhu, G.; Gao, Y.; Cheng, Q.; Cheng, X.: Synthesis of magnetic nickel ferrite/carbon sphere composite for levofloxacin elimination by activation of persulfate. *Separat. Purif. Technol.* **215**, 528–539 (2019)
31. Xiang, B.; Ling, D.; Lou, H.; Gu, H.: 3D hierarchical flower-like nickel ferrite/manganese dioxide toward lead (II) removal from aqueous water. *J. Hazard. Mater.* **325**, 178–188 (2017)
32. Pund, S.N.; Nagwade, P.A.; Nagawade, A.V.; Thopate, S.R.; Bagade, A.V.: Preparation techniques for zinc ferrites and their applications: a review. *Mater. Today Proc.* **2022**
33. Dong, W.; Wu, S.; Chen, D.; Jiang, X.; Zhu, C.: Preparation of α -Fe₂O₃ nanoparticles by sol-gel process with inorganic iron salt. *Chem. Lett.* **29**, 496–497 (2000)
34. Liu, J.; Yang, S.; Wu, W.; Tian, Q.; Cui, S.; Dai, Z.; Ren, F.; Xiao, X.; Jiang, C.: 3D flowerlike α -Fe₂O₃@TiO₂ core-shell nanostructures: general synthesis and enhanced photocatalytic performance. *ACS Sustain. Chem. Eng.* **3**, 2975–2984 (2015)
35. Lakhera, S.K.; Watts, A.; Hafeez, H.Y.; Neppolian, B.: Interparticle double charge transfer mechanism of heterojunction α -Fe₂O₃/Cu₂O mixed oxide catalysts and its visible light photocatalytic activity. *Catal. Today* **300**, 58–70 (2018)
36. Patil, J.Y.; Nadargi, D.Y.; Gurav, J.L.; Mulla, I.S.; Suryavanshi, S.S.: Synthesis of glycine combusted NiFe₂O₄ spinel ferrite: a highly versatile gas sensor. *Mat. Lett.* **124**, 144–147 (2014)
37. Hu, Y.; Wang, H.; Liu, D.; Lin, G.; Wan, J.; Jiang, H.; Lai, X.; Hao, S.; Liu, X.: Lychee-like ZnO/ZnFe₂O₄ core-shell hollow microsphere for improving acetone gas sensing performance. *Ceram. Int.* **46**, 5960–5967 (2020)
38. Su, J.; Shang, Q.; Guo, T.; Yang, S.; Wang, X.; Ma, Q.; Guan, H.; Xu, F.; Tsang, S.C.: Construction of heterojunction ZnFe₂O₄/ZnO/Ag by using ZnO and Ag nanoparticles to modify ZnFe₂O₄ and its photocatalytic properties under visible light. *Mater. Chem. Phys.* **219**, 22–29 (2018)
39. Sonker, R.K.; Sabhajeet, S.R.; Yadav, B.C.: TiO₂-PANI nanocomposite thin film prepared by spin coating technique working as room temperature CO₂ gas sensing. *J. Mater. Sci. Mater. Electron.* **27**, 11726–11732 (2016)
40. Philip, J.; Gnanaprakash, G.; Panneerselvam, G.; Antony, M.P.; Jayakumar, T.; Raj, B.: Effect of thermal annealing under vacuum on the crystal structure, size, and magnetic properties of ZnFe₂O₄ nanoparticles. *J. Appl. Phys.* **102**, 054305 (2007)
41. Hamdeh, H.H.; Ho, J.C.; Oliver, S.A.; Willey, R.J.; Oliveri, G.; Busca, G.: Magnetic properties of partially-inverted zinc ferrite aerogel powders. *J. Appl. Phys.* **81**, 1851–1857 (1997)
42. Thommes, M.: Physical adsorption characterization of nanoporous materials. *Chem. Ing. Tech.* **82**, 1059–1073 (2010)
43. Barick, K.C.; Singh, S.; Aslam, M.; Bahadur, D.: Porosity and photocatalytic studies of transition metal doped ZnO nanoclusters. *Microporous Mesoporous Mater.* **134**, 195–202 (2010)
44. Hou, X.; Xue, S.; Liu, M.; Shang, X.; Fu, Y.; He, D.: Hollow irregular octahedra-like NiCo₂O₄ cages composed of mesoporous nanosheets as a superior anode material for lithium-ion batteries. *Chem. Eng. J.* **350**, 29–36 (2018)
45. Abhilash, M.R.; Akshatha, G.; Srikantaswamy, S.: Photocatalytic dye degradation and biological activities of the Fe₂O₃/Cu₂O nanocomposite. *RSC Adv.* **9**, 8557–8568 (2019)
46. Babji, P.; Rao, V.L.: Catalytic reduction of 4-nitrophenol to 4-aminophenol by using Fe₂O₃-Cu₂O-TiO₂ nanocomposite. *Int. J. Chem. Stud.* **4**, 123–127 (2016)



47. Aksoy, S.; Caglar, Y.: Synthesis of Mn doped ZnO nanopowders by MW-HTS and its structural, morphological and optical characteristics. *J. Alloys Comp.* **781**, 929–935 (2019)
48. Doostmohammadi, A.; Monshi, A.; Salehi, R.; Fathi, M.H.; Seyed-jafari, E.; Shafiee, A.; Soleimani, M.: Cytotoxicity evaluation of 63s bioactive glass and bone-derived hydroxyapatite particles using human bone-marrow stem cells. *Biomed. Pap. Fac. Med. Palacka Univ. Olomouc Czech Republic* **155**, 323–326 (2011)
49. Chalasani, R.; Vasudevan, S.: Cyclodextrin-functionalized Fe₃O₄@TiO₂: reusable, magnetic nanoparticles for photocatalytic degradation of endocrine-disrupting chemicals in water supplies. *ACS Nano* **7**, 4093–4104 (2013)
50. Kakavandi, B.; Jonidi Jafari, A.; Rezaei Kalantary, R.; Nasser, S.; Esrafil, A.; Gholizadeh, A.; Azari, A.: Simultaneous adsorption of lead and aniline onto magnetically recoverable carbon: Optimization, modeling and mechanism. *J. Chem. Technol. Biotechnol.* **91**, 3000–3010 (2016)
51. Ahmadpour, N.; Sayadi, M.H.; Sobhani, S.; Hajiani, M.: Photocatalytic degradation of model pharmaceutical pollutant by novel magnetic TiO₂@ZnFe₂O₄/Pd nanocomposite with enhanced photocatalytic activity and stability under solar light irradiation. *J. Environ. Manag* **271**, 110964 (2020)
52. Marusak, L.A.; Messier, R.; White, W.B.: Optical absorption spectrum of hematite, α -Fe₂O₃ near IR to UV. *J. Phys. Chem. Solids* **41**, 981–984 (1980)
53. Jo, W.-K.; Selvam, N.C.S.: Synthesis of GO supported Fe₂O₃-TiO₂ nanocomposites for enhanced visible-light photocatalytic applications. *Dalton Trans.* **44**, 16024–16035 (2015)
54. Zotti, G.; Schiavon, G.; Zecchin, S.; Casellato, U.: Electrodeposition of amorphous Fe₂O₃ films by reduction of iron perchlorate in acetonitrile. *J. Electrochem. Soc.* **145**, 385 (1998)
55. Dghoughi, L.; Elidrissi, B.; Bernede, C.; Addou, M.; Lamrani, M.A.; Regragui, M.; Erguig, H.: Physico-chemical, optical and electrochemical properties of iron oxide thin films prepared by spray pyrolysis. *Appl. Surf. Sci.* **253**, 1823–1829 (2006)
56. Beermann, N.; Vayssieres, L.; Lindquist, S.E.; Hagfeldt, A.: Photoelectrochemical studies of oriented nanorod thin films of hematite. *J. Electrochem. Soc.* **147**, 2456 (2000)
57. Goyal, R.N.; Pandey, A.K.; Kaur, D.; Kumar, A.: Fabrication of α -Fe₂O₃ nanopowder modified glassy carbon electrode for applications in electrochemical sensing. *J. Nanosci. Nanotechnol.* **9**, 4692–4699 (2009)
58. Hayes, D.; Hadt, R.G.; Emery, J.D.; Cordones, A.A.; Martinson, A.B.F.; Shelby, M.L.; Fransted, K.A.; Dahlberg, P.D.; Hong, J.; Zhang, X.: Electronic and nuclear contributions to time-resolved optical and X-ray absorption spectra of hematite and insights into photoelectrochemical performance. *Energy Environ. Sci.* **9**, 3754–3769 (2016)
59. Rufus, A.; Sreeju, N.; Philip, D.: Synthesis of biogenic hematite (α -Fe₂O₃) nanoparticles for antibacterial and nanofluid applications. *RSC Adv.* **6**, 94206–94217 (2016)
60. Akl, A.A.: Optical properties of crystalline and non-crystalline iron oxide thin films deposited by spray pyrolysis. *Appl. Surf. Sci.* **233**, 307–319 (2004)
61. Jaramillo, T.F.; Baeck, S.-H.; Kleiman-Shwarsstein, A.; Choi, K.-S.; Stucky, G.D.; McFarland, E.W.: Automated electrochemical synthesis and photoelectrochemical characterization of Zn_{1-x}Co_xO thin films for solar hydrogen production. *J. Combinat. Chem.* **7**, 264–271 (2005)
62. Shalaby, N.H.; Elsalamony, R.A.; El Naggar, A.M.A.: Mesoporous waste-extracted SiO₂-Al₂O₃-supported Ni and Ni-H₃PW₁₂O₄₀ nano-catalysts for photo-degradation of methyl orange dye under UV irradiation. *New J. Chem.* **42**, 9177–9186 (2018)
63. El-Salamony, R.A.; Gobara, H.M.; Younis, S.A.; Moustafa, Y.M.: Zn⁺²-doped x-Ti-SiO₂ tricomposites for enhancement the photocatalytic degradation of phenol under UV irradiation. *J. Solgel Sci. Technol.* **83**, 422–435 (2017)
64. Mathevala, L.E.; Noto, L.L.; Mothudi, B.M.; Dhlamini, M.S.: Structural and optical properties of α -Fe₂O₃ nanoparticles, influence by holmium ions. *Physica B Cond. Matt.* **535**, 258–261 (2018)
65. El-Salamony, R.A.; Morsi, R.E.; Alsabagh, A.M.: Preparation, stability and photocatalytic activity of titania nanofluid using gamma irradiated titania nanoparticles by two-step method. *J. Nanofluids* **4**, 442–448 (2015)
66. Rashid, J.; Barakat, M.A.; Ruzmanova, Y.; Chianese, A.: Fe₃O₄/SiO₂/TiO₂ nanoparticles for photocatalytic degradation of 2-chlorophenol in simulated wastewater. *Environ. Sci. Pollut. Res.* **22**, 3149–3157 (2015)
67. Salker, A.V.; Gokakakar, S.D.: Solar assisted photo-catalytic degradation of Amido Black 10B over cobalt, nickel and zinc metalloporphyrins. 2009.

